REPORT DOCUMENTATION PAGE

Form Approved OMB NO. 0704-0188

1. REPORT DATE (DD-MM-YYYY)	2. REPORT TYPE	3. DATES COVERED (From - To)
12-07-2012	Conference Proceeding	-

4. TITLE AND SUBTITLE

SPARSE MODELING FOR HYPERSPECTRAL IMAGERY WITH LIDAR DATA FUSION FORSUBPIXEL MAPPING

5a. CONTRACT NUMBER
W911NF-11-1-0084

5b. GRANT NUMBER

5c. PROGRAM ELEMENT NUMBER
611102

6. AUTHORS

Alexey Castrodad, Timothy Khuon, Robert Rand, Guillermo Sapiro

5d. PROJECT NUMBER

5e. TASK NUMBER

5f. WORK UNIT NUMBER

7. PERFORMING ORGANIZATION NAMES AND ADDRESSES

University of Minnesota - Minneapolis
Sponsored Projects Administration
450 McNamara Alumni Center
Minneapolis, MN 55455 -2009

8. PERFORMING ORGANIZATION REPORT NUMBER

9. SPONSORING/MONITORING AGENCY NAME(S) AND ADDRESS(ES)

U.S. Army Research Office
P.O. Box 12211
Research Triangle Park, NC 27709-2211

10. SPONSOR/MONITOR'S ACRONYM(S)
ARO

11. SPONSOR/MONITOR'S REPORT NUMBER(S)
59626-MA.10

12. DISTRIBUTION AVAILIBILITY STATEMENT

Approved for public release; distribution is unlimited.

13. SUPPLEMENTARY NOTES

The views, opinions and/or findings contained in this report are those of the author(s) and should not contrued as an official Department of the Army position, policy or decision, unless so designated by other documentation.

14. ABSTRACT

Several studies suggest that the use of geometric features along with spectral information improves the classification and visualization quality of hyperspectral imagery. These studies normally make use of spatial neighborhoods of hyperspectral pixels for extracting these geometric features. In

15. SUBJECT TERMS

sparse modeling, HSI, LIDAR, sub-pixel

16. SECURITY CLASSIFICATION OF:			17. LIMITATION OF ABSTRACT	15. NUMBER OF PAGES	19a. NAME OF RESPONSIBLE PERSON
a. REPORT	b. ABSTRACT	c. THIS PAGE			Guillermo Sapiro
UU	UU	UU	UU		19b. TELEPHONE NUMBER 612-625-1343

Report Title

SPARSE MODELING FOR HYPERSPECTRAL IMAGERY WITH LIDAR DATA FUSION FORSUBPIXEL MAPPING

ABSTRACT

Several studies suggest that the use of geometric features along with spectral information improves the classification and visualization quality of hyperspectral imagery. These studies normally make use of spatial neighborhoods of hyperspectral pixels for extracting these geometric features. In this work, we merge point cloud Light Detection and Ranging (LiDAR) data and hyperspectral imagery (HSI) into a single sparse modeling pipeline for subpixel mapping and classification. The model accounts for material variability and noise by using learned dictionaries that act as spectral endmembers. Additionally, the estimated abundances are influenced by the LiDAR point cloud density, particularly helpful in spectral mixtures involving partial occlusions and illumination changes caused by elevation differences. We demonstrate the advantages of the proposed algorithm with co-registered LiDAR-HSI data.

Conference Name: IEEE International Geoscience and Remote Sensing Symposium

Conference Date: July 15, 2012

SPARSE MODELING FOR HYPERSPECTRAL IMAGERY WITH LIDAR DATA FUSION FOR SUBPIXEL MAPPING

Alexey Castrodad[1,2]*, Timothy Khuon*[1]*, Robert Rand*[1]*, and Guillermo Sapiro*[2]

1. NGA, 2. University of Minnesota, ECE Department

ABSTRACT

Several studies suggest that the use of geometric features along with spectral information improves the classification and visualization quality of hyperspectral imagery. These studies normally make use of spatial neighborhoods of hyperspectral pixels for extracting these geometric features. In this work, we merge point cloud Light Detection and Ranging (LiDAR) data and hyperspectral imagery (HSI) into a single sparse modeling pipeline for subpixel mapping and classification. The model accounts for material variability and noise by using learned dictionaries that act as spectral endmembers. Additionally, the estimated abundances are influenced by the LiDAR point cloud density, particularly helpful in spectral mixtures involving partial occlusions and illumination changes caused by elevation differences. We demonstrate the advantages of the proposed algorithm with co-registered LiDAR-HSI data.

1. INTRODUCTION

HSI sensors acquire images in which each pixel contains narrowly spaced measurements of the electromagnetic spectrum, allowing spectroscopic analysis. The data acquired by these spectrometers play significant roles in biomedical, environmental, land-survey, and defense applications. It contains very high spectral resolution, at the expense of less (spatial) geometrical information. There are numerous intrinsic challenges associated with effective ground mapping and characterization applications when using overhead HSI, see for example [1–3]. These are noise and sensor artifacts, complicated energy interaction schemes, intra-class variability, and spectral mixing. Consider for example a region in a scene where there are trees partially occluding a road. These elevation differences cause single pixels to have energy reflected from both the tree leaves and the road, and are also affected by shade. This problem motivates the use of additional information sources for potentially mitigating these effects. LiDAR point cloud data provides precise range information on a three dimensional space. In particular, LiDAR sensors acquire one or multiple elevation measurements per single (discretized) ground planar coordinate. When these point cloud data are co-registered with the hyperspectral pixels, they give insight into identifying structural changes, including partial occlusions within a spectral pixel. This advantage has motivated several works to use LiDAR and HSI for improved classification. For example, in [4], the authors used depth information from LiDAR as part of the parametrization required for a bio-optical model to perform underwater benthic mapping. In [5], the authors studied the possible correlations of the surface roughness and minerals' spectral content. In [6], LiDAR information was used to better localize small targets by first performing a background/foreground segmentation on the elevation map, and then using regions of interest based on height for improved small target detection. It has also been applied for obtaining higher discrimination between savanna tree species by the use of hand crafted decision trees [7–9]. With the exception of [4], these works require careful hand tuning of decision operations, and require a sequential processing of LiDAR and HSI. Our framework, described in sections 2 and 3, drifts away from these approaches because the model *simultaneously* uses information from both data sources to estimate the pixels spectral abundance (and corresponding labels). The HSI cube is expressed as a sparse linear combination of learned sources (dictionary atoms), giving meaningful material abundance estimates, without explicit dimension reduction or subspace projection preprocessing steps. We impose spatial coherence in the sparse modeling-based classification. This efficiently fuses spectral (HSI) and structural (LiDAR) information by incorporating local and nonlocal connectivities between local regions in the scene, leading to a grouping criteria that induces a robust and stable abundance mapping. This will be illustrated with real data examples in Section 4.

2. SPARSE MODELING HSI

Let each measured pixel $\mathbf{y} = [y_1, y_2, ..., y_b]$ in the hyperspectral image be a vector valued function, $y_i : \Re^2 \rightarrow \Re^+, 1 \leq i \leq b$, where b denotes the number of spectral bands. We stack these pixels in matrix format as $\mathbf{Y} = [\mathbf{y}_1, ..., \mathbf{y}_n] \in \Re^{b \times n}$,

Work partially supported by NGA, ONR, ARO, NSF, DARPA, and AFOSR (NSSEFF). Alexey Castrodad and Guillermo Sapiro are with the Department of Electrical and Computer Engineering, University of Minnesota, Minneapolis, MN, 55455 USA e-mail: {castr103, guille}@umn.edu. Alexey Castrodad, Timothy Khuon, and Robert Rand are with the National Geospatial-Intelligence Agency.

where n is the total number of available pixels distributed spatially. All the entries of this matrix are nonnegative. In addition, we assume that the measured energy $\mathbf{Y}$ at the sensor is proportional to the area covered by the dictionary of materials $\mathbf{\Psi}$ and the reflectivity of the media, which can be modeled as the linear system $\mathbf{Y} = \mathbf{\Psi}\mathbf{A} + \mathbf{N}$, where $\mathbf{N}$ is additive noise with bounded energy ($\|\mathbf{N}\|_F^2 \leq \sigma^2$), $\mathbf{\Psi} \in \Re^{b\times k}$ is a dictionary (soon to be learned), and $\mathbf{A} \in \Re^{k\times n}$ is the associated matrix of coefficients representing the mixture of dictionary atoms when composing the data. The goal is to learn the dictionary $\mathbf{\Psi}$ representing the materials, and their proper combination $\mathbf{A}$, just from $\mathbf{Y}$ (unsupervised case) or from $\mathbf{Y}$ and a labeled library of real data (supervised case). We follow for this the modeling procedure from [10]. Assuming there are C materials, this model aims to learn a block-structured dictionary of materials, where the $j-th$ block is representative of the $j-th$ material, $j \in [1, ..., C]$. Learning each material subdictionary can be summarized as solving the following biconvex optimization problem,

$$\begin{aligned}(\mathbf{\Psi}^{j*}, \mathbf{A}^{j*}) &= \arg\min_{(\mathbf{\Psi}^j, \mathbf{A}^j)\succeq 0} \sum_{i=1}^{n_j} \{\frac{1}{2}\|\mathbf{\Psi}^j \mathbf{a}_i^j - \mathbf{y}_i^j\|_2^2 \\ &\quad +\lambda\|\mathbf{a}_i^j\|_1\} \\ &= \arg\min_{(\mathbf{\Psi}^j, \mathbf{A}^j)\succeq 0} \sum_{i=1}^{n_j} \mathcal{H}(\mathbf{y}_i^j; \mathbf{\Psi}^j, \mathbf{a}_i^j), \quad (1)\end{aligned}$$

where there are n_j pixels $\mathbf{y}_i^j$ pertaining to the $j-th$ class, $\mathbf{A} = [\mathbf{a}_1, ..., \mathbf{a}_{n_j}] \in \Re^{k_j \times n_j}$ (each class-dictionary can potentially have a different size k_j), and $\lambda \geq 0$ is a parameter that controls the trade-off between reconstruction quality and sparsity. After learning the material dictionaries in a separate fashion, the structured dictionary $\mathbf{\Psi} = [\mathbf{\Psi}^1, ..., \mathbf{\Psi}^C]$ is assembled and used for solving for the corresponding abundance coefficients originated from a linear combination of atoms from $\mathbf{\Psi}$:

$$\mathbf{A}^* = \underset{\mathbf{A}\succeq 0}{\operatorname{argmin}} \quad \sum_{i=1}^{n} \mathcal{H}(\mathbf{y}_i, \mathbf{\Psi}; \mathbf{a}_i). \quad (2)$$

Equations (1) and (2) provide sufficient information for HSI subpixel mapping. If we define a per-block sum operator $\mathbf{M} \in \Re^{C\times k}$ as $\mathbf{M} = \begin{bmatrix} \mathbf{1}^1 & \mathbf{0} & \cdots & \mathbf{0} \\ \mathbf{0} & \mathbf{1}^2 & & \\ \vdots & & \ddots & \\ \mathbf{0} & \cdots & & \mathbf{1}^C \end{bmatrix}$, where $\mathbf{1}^j \in \Re^{1\times k_j}$ is a vector of ones corresponding to the number k_j of atoms per subdictionary, then, a mapping $f(\mathbf{y}) : \Re^b \to \Re^C$ is $f(\mathbf{y}) = \mathbf{M}\mathbf{a}$, corresponds to the ℓ_1-norm per material, yielding fractional abundance estimates (see [10] for details).

3. HSI-LIDAR FUSION

We want to minimize the effects of partial occlusions in the scene, and since there could be more than one LiDAR return sample per discrete spatial coordinate,[1] we pick the data sample with the minimum elevation value per discrete spatial (x, y)-coordinate. Similarly, we use the average intensity value per discrete spatial (x, y)-coordinate. We concatenate these two values into a single vector $\mathbf{r}_i \in \Re^2, \forall i \in [1, ..., n]$. The purpose behind this procedure is to enforce spatial homogeneity in the spectral abundance estimates in the regions where the LiDAR's active signal reached farthest.

Up to this point, each pixel is treated independently from each other. To exploit the structural scene information available from LiDAR, one can enforce the estimation of the abundance coefficients $\mathbf{A}$ to be influenced by the spatial geometry of the point cloud data, hence inducing spatial and spectral coherence in the abundance estimation process. This coherence will depend both on the pixels' spectral shape *and* the geometry of LiDAR data. Let $\mathcal{F}$ be a collaborative term on the coefficients,

$$\mathcal{F}(\mathbf{M}, \mathbf{w}_i; \mathbf{a}_i) = \|(\mathbf{M}\mathbf{a}_i - \sum_{l\in\eta} w_{il}\mathbf{M}\mathbf{a}_l)\|_1, \quad (3)$$

where η denotes a predefined neighborhood associated to the $i-th$ pixel. $\mathcal{F}$ will highly depend on the weighting function w_{il}. An example of such a function is

$$w_{il} = \frac{1}{Z_i}(\alpha \exp^{-(\frac{\|\mathbf{y}_i - \mathbf{y}_l\|_2^2}{\sigma_s^2})} + (1-\alpha)\exp^{-(\frac{\|\hat{\mathbf{r}}_i - \hat{\mathbf{r}}_l\|_2^2}{\sigma_r^2})}), \quad (4)$$

where $\alpha \in [0, 1]$ controls the contribution of each data source, Z_i is a pixel-dependent normalization constant such that $\sum_{l\in\eta} w_{il} = 1$, $\hat{\mathbf{r}}$ is a vectorized spatial window (patch) around each of the concatenated LiDAR range and intensity samples $\mathbf{r}$, and σ_s^2, σ_r^2 are density parameters for the spectral and range content, respectively, controlling the width of the weighting function (here set to be the average of the data's pairwise Euclidean distance, either local for each pixel or global for the whole data). This weighting function is close to 1 if the both the hyperspectral pixels and the LiDAR local coordinates are homogeneous, and 0 otherwise.

Finally, our proposed mapping approach remounts to solving the optimization problem

$$\mathbf{A}^* = \underset{\mathbf{A}\succeq 0}{\operatorname{argmin}} \quad \sum_{i=1}^{n} \{\mathcal{H}(\mathbf{Y}, \mathbf{\Psi}; \mathbf{a}_i) + \beta\mathcal{F}(\mathbf{M}, \mathbf{w}_i; \mathbf{a}_i)\}, \quad (5)$$

where $\beta \geq 0$ is a parameter controlling the amount of collaboration between LiDAR and HSI data samples. Notice that $\mathcal{F}(\mathbf{M}, \mathbf{w}_i; \mathbf{a}_i)$ introduces a variable coupling. We efficiently solve this using the Split Bregman method [11] and primal

[1] In this work, we exploit the LiDAR's point cloud data. Rasterized data could also be used as an alternative data source.

decomposition. First, we reformulate Equation (5) as to solving the following constrained optimization problem (for each pixel):

$$\min_{\mathbf{a}_i \succeq 0} \sum_{i=1}^{n} \{\mathcal{H}(\mathbf{y}_i, \mathbf{\Psi}; \mathbf{a}_i) + \|\mathbf{v}_i\|_1 + \|\mathbf{u}_i\|_1\}$$
$$\text{s.t.} \quad \mathbf{v}_i = \mathbf{a}_i, \mathbf{u}_i = \mathbf{M}\mathbf{a}_i - \sum_{l \in \eta} w_l \mathbf{M}\mathbf{a}_l, \forall i \in [1, n]. \quad (6)$$

Second, the constraints are enforced by applying an Augmented Lagrangian formulation:

$$\mathcal{L}(\mathbf{a}, \mathbf{v}, \mathbf{u}, \mathbf{b}, \mathbf{c}) = \mathcal{H}(\mathbf{y}, \mathbf{\Psi}; \mathbf{a}) + \|\mathbf{v}\|_1 + \|\mathbf{u}\|_1$$
$$+\lambda < \mathbf{b}, \mathbf{a} - \mathbf{v} > + \beta < \mathbf{c}, \mathbf{g} - \mathbf{u} > + \frac{\lambda}{2}\|\mathbf{a} - \mathbf{v}\|_2^2$$
$$+ \frac{\beta}{2}\|\mathbf{g} - \mathbf{u}\|_2^2, \quad (7)$$

where $\mathbf{g} = \sum_{l \in \eta} w_l \mathbf{M}\mathbf{a}_l$, and we maximize for the dual variables $\mathbf{b}$ and $\mathbf{c}$, and minimize for $\mathbf{a}, \mathbf{v}$, and $\mathbf{u}$. Finally, the proposed abundance mapping algorithm is reduced to solving the following subproblems independently:

$$\mathbf{a}^{t+1} = \operatorname{argmin}_{\mathbf{a} \succeq 0} \{\frac{1}{2}\|\mathbf{\Psi}\mathbf{y} - \mathbf{a}^t\|_2^2 + \frac{\lambda}{2}\|\mathbf{a}^t - \mathbf{v}^t + \mathbf{b}^t\|_2^2$$
$$+ \frac{\beta}{2}\|\mathbf{M}\mathbf{a}^t - \mathbf{g}^t + \mathbf{c}^t\|_2^2\}, \quad (8)$$
$$\mathbf{v}^{t+1} = \operatorname{argmin}_{\mathbf{v} \succeq 0} \{\|\mathbf{v}^t\|_1 + \frac{\lambda}{2}\|\mathbf{a}^{t+1} - \mathbf{v}^t + \mathbf{b}^t\|_2^2\}, \quad (9)$$
$$\mathbf{u}^{t+1} = \operatorname{argmin}_{\mathbf{u} \succeq 0} \{\|\mathbf{u}^t\|_1 + \frac{\beta}{2}\|\mathbf{M}\mathbf{a}^{t+1} - \mathbf{g}^{t+1} + \mathbf{c}^t\|_2^2\}, \quad (10)$$
$$\mathbf{b}^{t+1} = \mathbf{b}^t - \mathbf{v}^{t+1} + \mathbf{a}^{t+1}, \quad (11)$$
$$\mathbf{c}^{t+1} = \mathbf{c}^t - \mathbf{g}^{t+1} + \mathbf{M}\mathbf{a}^{t+1} - \mathbf{u}^{t+1}. \quad (12)$$

These subproblems are solved until convergence in the ℓ_2-norm of $\mathbf{a}$, which takes about 50 iterations in our experiments. Note that the subproblems can be solved simply via inversion (Equation (8)), shrinking (equations (9) and (10)), and explicitly (equations (11) and (12)), see [11] for more details. [2] This concludes the subpixel modeling procedure. Full-pixel labeling derives directly by selecting the $i-th$ pixel's label corresponding to the maximum element of $\mathbf{M}\mathbf{a}_i$. We now proceed with experiments supporting our model.

4. EXPERIMENTS

In this section, we validate our model by applying it to co-registered HSI and LiDAR data. This dataset consists of an airborne data collection over Gulfport, Mississippi, in November, 2010. The scene is composed of low density urban and coastal regions. The HSI data was acquired with a CASI-1500 sensor, with a spectral range of 375-1050 nm in 72 bands. The LiDAR data was acquired with an Optech ALTM Gemini sensor, operating at a wavelength of 1064 nm. These data are co-registered at 1 m spatial resolution, with a total of 324×500 pixels. We analyze two scenarios: supervised and unsupervised mapping. On both scenarios, we compare the mapping results with and without LiDAR information, hence highlighting the benefits of the proposed joint modeling scheme. We selected $\lambda = \frac{0.5}{\sqrt{b}}$, and $\alpha = 0.9$. The neighborhood η for each pixel patch of 3×3,[3] was composed using 4 spatially connected overlapping patches and the 4 most similar patches across the entire image spatial domain. All experimental results are illustrated in Figure 1. Subfigures 1(a) and 1(b) show false color composites from the scene for the LiDAR and HSI data, respectively.

On a supervised setting, we used *a priori* averaged spectra from 11 materials. These materials are labeled: *C1: canvas, C2: fabric #1, C3: fabric #2, C4: trees, C5: healthy grass, C6: grounds, C7: asphalt, C8: red roof, C9: brown roof, C10: tan roof,* and *C11: sand*. These spectra served as the dictionary $\mathbf{\Psi}$. We processed the data by using the proposed mapping algorithm for $\beta = 0$ and $\beta = \frac{0.1}{\sqrt{b}}$, that is, with and without fusion. Subfigures 1(e) and 1(f) show these full-pixel mappings. Notice how the estimates are smoother in Subfigure 1(f), for instance, a more homogeneous region around the red building on the lower left of the image. Also, there are *grounds* pixels that are incorrectly labeled as *concrete*, and are correctly labeled by activating the fusion term in the proposed model.

On an unsupervised setting, we followed the endmember learning procedure from [10]. Basically, $\mathbf{\Psi}$ is initialized using a single estimated spectra for each of the C materials using a nonnegative matrix factorization, where the abundance coefficients are constrained to sum to one, and continues adding atoms to each subdictionary $\mathbf{\Psi}^j$ until the change in reconstruction error reaches 1×10^{-4}. We applied the proposed fusion algorithm after learning $\mathbf{\Psi}$ with $C = 11$ materials (labeled as U's in Figure 1). In Subfigure 1(d), we show a spectral sample reconstructed using the proposed model corresponding to a small tree under the shade from a taller building. This sample is compared with the original HSI sample, and the average (supervised) spectra from the *trees* class. The fused spectra shows a higher amplitude in the channels corresponding to green and red wavelength. This is due to the collaboration effect of the proposed model, enforcing homogeneous regions from LiDAR and HSI to have similar abundance values. Subfigures 1(g) and 1(h) illustrate the full-pixel mappings with and without fusion. Again, we observe a smoother mapping in Subfigure 1(h). Finally, in Subfigure 1(c), we illustrate the false color composite after applying the proposed model (in an unsupervised manner). Notice how the effect of shading caused by the sun in the HSI scene is signif-

[2] The nonnegativity constraint is enforced by projecting into nonnegative numbers.

[3] Spatial patches were used for the LiDAR depth and intensity data. Single pixels were used for HSI data.

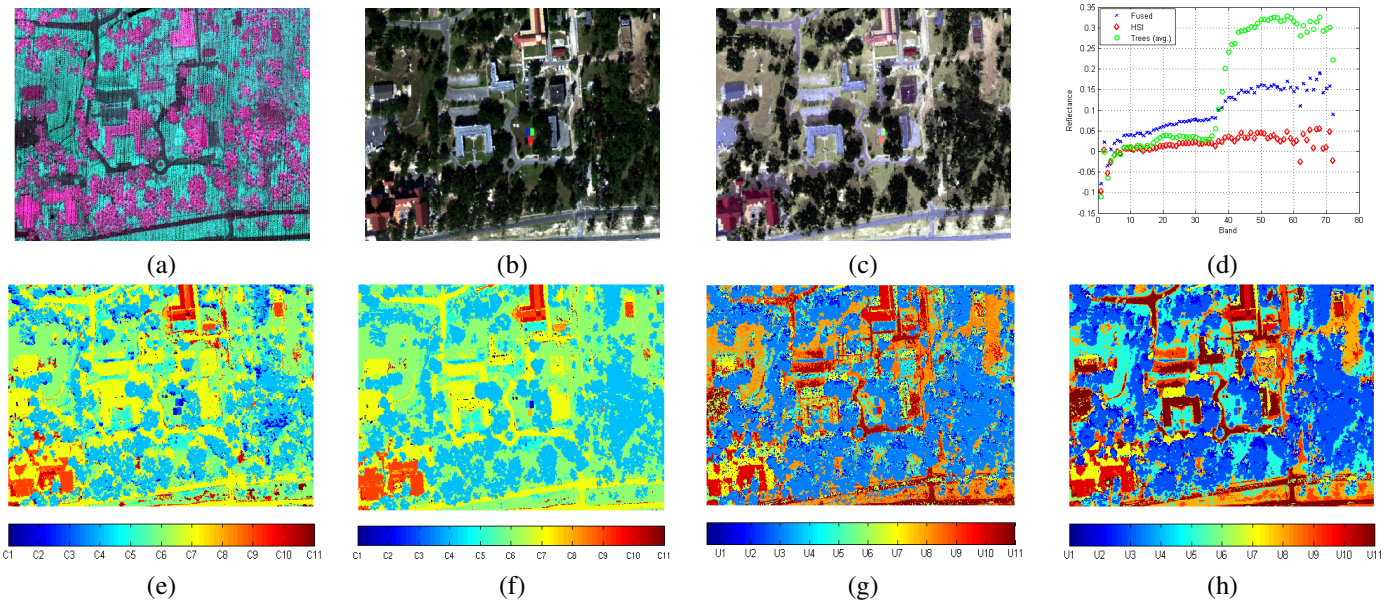

Fig. 1. Fusion of HSI and LiDAR data from the Gulfport scene. (a) Depth-intensity-average map from LiDAR. (b) False color RGB from hyperspectral scene. (c) False color RGB from HSI-LiDAR fused scene. (d) Influence of LiDAR data into spectral estimation, pixel (162,160). (e) Supervised spectral mapping, no fusion. (f) Supervised spectral spectral mapping with fusion. (g) Unsupervised spectral mapping, no fusion. (h) Unsupervised spectral mapping with fusion. (This is a color figure.)

icantly alleviated in the new representation.

5. CONCLUSION

We presented a sparse modeling algorithm for source separation and classification using hyperspectral imagery and LiDAR. The range information from LiDAR data provides rich structural information, and is used to enhance the classification performance in HSI. An affinity function that combines the spectral information along with the spatial information in LiDAR is incorporated in the model to promote collaboration between the two data sources. The proposed unsupervised algorithm learns a structured dictionary representing the spectral sources/endmembers, and expresses each pixel as a sparse linear combination of the dictionary atoms. These coefficients provide information for spectral abundance mapping and classification. We performed experiments using real HSI/LiDAR data illustrating the advantages of multimodal information for remote sensing applications. In particular, we showed how using this model alleviates the effects of partial occlusions caused by elevation differences and shading.

6. REFERENCES

[1] Chein-I Chang, *Hyperspectral Data Exploitation: Theory and Applications*, John Wiley and Sons, 2007.

[2] D. A. Landgrebe, *Signal Theory Methods in Multispectral Remote Sensing*, John Wiley and Sons, 2003.

[3] A. Plaza, J. A. Benediktsson, J. W. Boardman, J. Brazile, L. Bruzzone, G. Camps-Valls, J. Chanussot, M. Fauvel, P. Gamba, A. Gualtieri, M. Marconcini, J. C. Tilton, and G. Trianni, "Recent advances in techniques for hyperspectral image processing," *Remote Sensing of Environment*, vol. 113, pp. 110122, 2009.

[4] M.C. Torres-Madronero, M. Velez-Reyes, and J.A. Goodman, "Fusion of hyperspectral imagery and bathymetry information for inversion of bioptical models," in *SPIE, Remote Sensing of the Ocean, Sea Ice, and Large Water Regions*, 2009.

[5] M. S. West and R. G. Resmini, "Hyperspectral imagery and LiDAR for geological analysis of Cuprite, Nevada," in *Society of Photo-Optical Instrumentation Engineers (SPIE) Conference Series*, 2009, vol. 7334.

[6] A. V. Kanaev, B. J. Daniel, J. G. Neumann, A. M. Kim, and K. R. Lee, "Object level HSI-LIDAR data fusion for automated detection of difficult targets," *Opt. Express*, vol. 19, no. 21, pp. 20916–20929, 2011.

[7] M.A. Cho, L. Naidoo, R. Mathieu, and G.P. Asner, "Mapping savanna tree species using carnegie airborne observatory hyperspectral data resampled to worldview-2 multispectral configuration," in *34th International Symposium on Remote Sensing of Environment*, 2011.

[8] L. Naidoo, M.A. Cho, R. Mathieu, and G.P. Asner, "Spectral classification of savanna tree species, in the greater kruger national park region using carnegie airborne observatory (cao) integrated hyperspectral and lidar data," in *1st AfricaGEO Conference, Cape Town*, 2011.

[9] D. Sarrazin, J.A. van Aardt, D.W. Messinger, and G.P. Asner, "Fusing waveform lidar and hyperspectral data for species-level structural assessment in savanna ecosystems," in *SPIE, Laser Radar Technology and Applications XV*, 2010.

[10] A. Castrodad, Z. Xing, J.B. Greer, E. Bosch, L. Carin, and G. Sapiro, "Learning discriminative sparse representations for modeling, source separation, and mapping of hyperspectral imagery.," *Geoscience and Remote Sensing, IEEE Transactions on*, vol. 49, no. 11, pp. 4263–4281, 2011.

[11] T. Goldstein and S. Osher, "The split Bregman method for l1-regularized problems," *SIAM Journal on Imaging Sciences*, vol. 2, no. 2, pp. 323–343, 2009.